# Photoluminescence of monoclinic Li$_3$AlF$_6$ crystals under vacuum ultraviolet and soft X-ray excitations

CrossMark

V.A. Pustovarov [a], I.N. Ogorodnikov [a], S.I. Omelkov [b,*], M.S. Molokeev [c,d], A.V. Kozlov [a], L.I. Isaenko [e,f]

[a] Ural Federal University, 19, Mira Street, 620002 Yekaterinburg, Russia
[b] Institute of Physics, University of Tartu, 14c, Ravila Street, 50411 Tartu, Estonia
[c] Kirensky Institute of Physics SB RAS, Akademgorodok 50, 660036 Krasnoyarsk, Russia
[d] Far Eastern State Transport University, 47, Serysheva Street, 680021 Khabarovsk, Russia
[e] Institute of Geology and Mineralogy SB RAS, 43, Russkaya Street, 630058 Novosibirsk, Russia
[f] Novosibirsk National Research University, 2, Pirogova Street, 630090 Novosibirsk, Russia

## ARTICLE INFO

## ABSTRACT

Using Bridgman technique we have grown monoclinic $\beta$-LiAF crystals suitable for optical studies, performed XRD-identification and Rietveld refinement of the crystal structure and carried out a photoluminescence study upon vacuum ultraviolet (VUV) and extreme ultraviolet (XUV)-excitations, using the low-temperature ($T$ = 7.2 K) time-resolved VUV-spectroscopy technique. The intrinsic PL emission band at 340–350 nm has been identified as due to radiative recombination of self-trapped excitons. The electronic structure parameters were determined: bandgap $E_g \approx 12.5$ eV, energy threshold for creation of unrelaxed excitons 11.8 eV $< E_n <$ 12.5 eV. The PL emission bands at 320–325 and 450 nm were attributed to luminescence caused by lattice defects. We have discovered an efficient excitation of PL emission bands in the energy range of interband transitions ($E_{ex} >$ 13.5 eV), as well as in the energy range of core transitions at 130 eV. We have revealed UV–VUV PL emission bands at 170 and 208 nm due to defects. A reasonable assumptions about the origin of the UV–VUV bands were discussed.

© 2015 Elsevier B.V. All rights reserved.

## 1. Introduction

Owing to a large energy bandgap, complex fluorides have many practical applications. However, Lithium Hexafluoroaluminate Li$_3$AlF$_6$ (LiAF) crystals are practically unknown as optical materials. LiAF is utilized as a water insoluble Aluminum source for use in oxygen-sensitive applications, such as metal production. In extremely low concentrations (ppm), fluoride compounds are used in health applications.

LiAF crystals exist in two basic modifications. $\alpha$-LiAF modification can be obtained by quenching a corresponding sample from temperatures above 600 °C to room temperature. The $\alpha$-LiAF crystal structure has been determined at room temperature in Ref. [1], and it possesses an orthorhombic $Pna2_1$ symmetry with lattice constants of $a$ = 9.510, $b$ = 8.2295, $c$ = 4.8762 Å. Each of the ten atoms in formula unit occupies fourfold-coordinated site. Almost regular AlF$_6$ octahedra are linked with Li ions, each of which has six neighboring F ions at a distance of 1.87–2.42 Å. Bond length Al–F is about 1.786–1.830 Å. While the pseudo-face-centered cubic array of AlF$_6$

octahedra in $\alpha$-LiAF looks similar to that of the mineral cryolite, its deviations from the ideal structure of cryolite are quite significant. LiAF transformation into an ideal cryolite structure can only occur at elevated temperature. Several polymorphic transformations were revealed in the temperature range between room temperature and its melting point ($T_{melt}$ = 783°) [2,3].

$\beta$-LiAF modification crystallizes only during slow cooling, it is isotypic to $\beta$-Li$_3$VF$_6$, and possesses monoclinic $C2/c$ symmetry with $a$ = 14.201(1), $b$ = 8.387(1), $c$ = 9.860(1) Å, and $\beta$ = 94.07(1)° [4]. Only a few research works have been devoted to the study of $\beta$-LiAF: among them, thermodynamic analysis of lithium cryolite in the LiAF–$A$F$_2$ ($A$ = Ca, Ba, Sr) systems [5]; study of the heat capacity of $\beta$-LiAF in the temperature range from 15 to 380 K [6]; electrical conductivity of low melting baths for aluminium electrolysis: the system Na$_3$AlF$_6$–LiAF–AlF$_3$ [7]; Li$^+$-ion conductivity of LiAF [8].

We are not aware of any research work on optical and luminescence properties of LiAF, whereas related Li$M$AlF$_6$ ($M$ = Ba, Ca, Sr) single crystals are much better studied in this regard. This applies not only to study of the crystal structure [9], but also to study of the luminescence and optical properties of both the undoped crystals [10–12], and crystals doped with Ce$^{3+}$ [13,14], Cr$^{3+}$ [15],

* Corresponding author.
  E-mail address: omelkovs@gmail.com (S.I. Omelkov).

and Pr$^{3+}$ [16]. Electronic properties of undoped Li$M$AlF$_6$ crystals have been studied experimentally using vacuum ultraviolet optical and luminescence spectroscopy [12,17], and X-ray photoelectron spectroscopy techniques [17]. *Ab initio* electronic structure calculations have been done for LiCaAlF$_6$ (LICAF) single crystals [18,19]. The other related crystals of LiBaF$_3$ are known as window materials in the ultraviolet (UV) and vacuum ultraviolet (VUV) wavelength regions [20], as well as a scintillator for thermal-neutron detection with optimal $n/\gamma$ discrimination [21].

The aim of this research work is to study luminescence and optical properties of undoped LiAF crystals using the method of low-temperature time-resolved luminescence spectroscopy upon selective photoexcitation by VUV synchrotron radiation. LiAF crystals were grown by the Bridgman method, XRD-analysis and Rietveld refinement were carried out to identify and clarify the crystal structure. Analysis of the experimental spectroscopy results is performed with consideration of known data on related crystals.

## 2. Experimental details

### 2.1. Time-resolved PL spectroscopy

The present study was carried out using three different experimental setups. Let us briefly describe the relevant parameters of these facilities.

The low-temperature luminescence spectroscopy in UV–VUV spectral range with the time resolution upon selective excitation in the soft X-ray (XUV) energy range was carried out using synchrotron radiation (SR) at BW3 channel (HASYLAB, DESY, Hamburg). SR pulses from the undulator was monochromatized by a Zeiss SX700 monochromator. Time-resolved photoluminescence (PL) emission spectra in the VIS–UV–VUV regions (140–500 nm) as well as PL decay kinetics curves were recorded using a 0.4 m vacuum monochromator (Seya-Namioka scheme) equipped with a microchannel plate-photomultiplier (MCP1645 Hamamatsu) [22]. The spectra were recorded in two independent time windows (TWs) set for detection of luminescence signal within 1.2–9.5 ns (TW$_1$) and 19–90 ns (TW$_2$) relative to the beginning of the SR pulse. The effective time resolution of the entire detection system was 250 ps. Time-integrated (TI) spectra were recorded within the full time range available between two sequential excitation pulses, viz. 192 ns. The measurements were performed in the ultra-high-vacuum chamber (up to $10^{-9}$ mbar) at $T$ = 7–8 K.

PL emission spectra, PL decay kinetics, and time-resolved PL excitation (PLE) spectra were recorded upon selective VUV-excitation at SUPERLUMI station (Channel I, HASYLAB, DESY, Hamburg) [23] using an ARC Spectra Pro-308i monochromator and cooled CCD camera. The PLE spectra were recorded in two independent TWs set for detection of luminescence signal within 0.6–2.9 ns (TW$_1$) and 58–72 ns (TW$_2$) relative to the beginning of the SR pulse. The time resolution of the entire detection system was 1 ns (FWHM). The full time range available between two sequential excitation pulses was 96 ns. The PL emission spectra were corrected to spectral sensitivity of the registration system.

In addition, PL emission spectra in the UV–VUV energy region were recorded upon VUV-excitation (6–12 eV) using the mobile luminescence set-up [22] attached to the branch-line FINEST of I3 beamline at MAX-lab, Lund [24]. The detection system is identical to the one used in XUV experiment at BW3 beamline. All the PL excitation spectra presented in this paper were corrected to an equal number of photons incident on the sample using sodium salicylate.

### 2.2. Samples preparation and XRD analysis

Li$_3$AlF$_6$ compound was obtained from LiF and AlF$_3$ powders (99.5%), which were annealed in vacuum at 200 °C during 5 h

before weighting. A glass-graphite crucible with a conic bottom was filled with the stoichiometric mixture of LiF and AlF$_3$ and placed into evacuated and hermetically sealed silica ampoule. The synthesis took place in a hot zone of Bridgman furnace at 900 °C during 1 h. When synthesis was finished, the ampoule was being moved from hot zone to warm one with a temperature of 600 °C with the rate of 0.5 mm/h. Thus polycrystalline boules of Li$_3$AlF$_6$ with grains up to $5 \times 5 \times 5$ mm$^3$ in size were obtained.

The powder diffraction data of Li$_3$AlF$_6$ for Rietveld analysis were collected at room temperature using a Bruker D8 ADVANCE powder diffractometer (Cu K$\alpha$ radiation) and linear VANTEC detector. The step size of 2$\Theta$ was 0.016°, and the counting time was 1 s per step. Rietveld refinement was performed using TOPAS 4.2 [25]. Almost all peaks were indexed by monoclinic cell (C2/c) with parameters close to previously published $\beta$-Li$_3$AlF$_6$ [4]. Two peaks at 2$\Theta \approx 20°$ and 2$\Theta \approx 26°$ could not be attributed to the main phase. Unfortunately, these two peaks do not give enough information for phase identification of impurity, but rough estimation of its fraction using intensities gave <3%. Therefore the crystal structure [4] was taken as starting model for the Rietveld refinement. Refinement was stable and gives quite low $R$-factors, Table 1, Fig. 1. Coordinates of atoms and main bond lengths are listed in Tables 2 and 3 respectively. Bond lengths Al–F are in usual range 1.772 (9)–1.862(8) Å, Li–F bond lengths span the wide range 1.66(3)–2.55(3) Å, and this is common situation for this compound [4]. Primitive unit cell contains two independent Al ions which form AlF$_6$ octahedra, five Li ions which form three LiF$_6$ octahedra, one LiF$_5$ tetragonal pyramid and one LiF$_4$ tetrahedron, Fig. 2. Each AlF$_6$ octahedra linked with LiF$_n$ polyhedra by nodes or edges with common F ions and, in summary, all polyhedra form *3D* network.

## 3. Time-resolved luminescence spectroscopy

### 3.1. Vacuum ultraviolet excitation

Fig. 3 shows PL emission spectra of LiAF crystals recorded at $T$ = 7.2 K upon VUV-excitation at different energies $E_{ex}$ ranging from 6.20 to 13.80 eV. The spectra comprised of several broad PL emission bands with maxima at 320–350 and 450 nm, and their relative intensities depend on the excitation energies $E_{ex}$. At $E_{ex}$ = 6.20 and 6.80 eV, PL emission bands peaking at 320–325 and 450 nm are almost comparable in intensity. At $E_{ex}$ = 9.48 eV, the emission intensity is reduced by a factor of about 4–5, but

**Table 1**
Most relevant parameters of processing and refinement for LiAF.

| Parameter | Value |
| --- | --- |
| Compound | Li$_3$AlF$_6$ |
| Molar mass, g/mol | 161.7950 |
| Symmetry group | $C2/c$ |
| $a$, Å | 14.2292(7) |
| $b$, Å | 8.4038(5) |
| $c$, Å | 9.8800(5) |
| $\beta$, grad | 94.078(2) |
| $V$, Å$^3$ | 1178.45(11) |
| $Z$ | 4 |
| 2$\Theta$-interval, grad | 5–110 |
| Number of reflections | 750 |
| Number of refined parameters | 95 |
| $R_{wp}$, % | 10.58 |
| $R_p$, % | 7.76 |
| $R_{exp}$, % | 8.00 |
| $\chi^2$ | 1.32 |
| $R_B$, % | 1.98 |

Note. The agreement indices ($R$ values) were defined in agreement with Ref. [49]: $R_{wp}$ is the weighted-profile $R$-value; $R_p$ is $R$-pattern; $R_{exp}$ is the statistically expected $R$-value; $R_B$ is the Bragg-intensity $R$-value; $\chi = R_{wp}/R_{exp}$ is the goodness of fit.
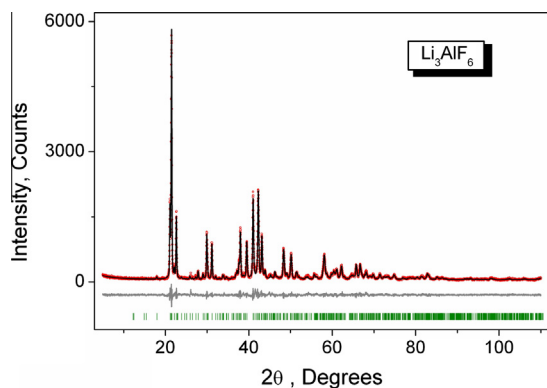
**Fig. 1.** Rietveld difference plot for LiAF crystal at $T = 300$ K.

there is only one broad PL emission band peaking at 340 nm. With further increase in $E_{ex}$, there is only one broad PL emission band peaking at 340–350 nm. It is worth noting that this PL emission band is the most intense one recorded upon excitation at $E_{ex} = 11.8$ eV and $E_{ex} > 13.5$ eV.

Fig. 4 shows PLE spectra of LiAF crystals recorded at $T = 7.2$ K monitoring emissions at 440 and 340 nm in either time-integrated regime (TI) or within time-windows $TW_1$ and $TW_2$. Time-integrated PLE spectrum recorded monitoring emission at $\lambda_m = 440$ nm comprises a low-intensity emission band at 6.14 eV, the dominant peak at 11.8 eV, deep minimum in the energy range of about 12.8 eV and, finally, the rise of the intensity in the energy region of $E_{ex} > 13.5$ eV. When changing $\lambda_m$ to 340 nm, PLE(TI) spectrum remains qualitatively the same, but the intensity ratio for the PL emission bands varies, Fig. 4. In the energy range of $E_{ex} > 13.5$ eV, PLE intensity increases, whereas the intensity of the 6.14 eV PLE-band decreases by a factor of about three. The time-resolved spectra $TW_1$ and $TW_2$ indicate that the PL decay kinetics should include nanosecond decay components with different lifetimes.

Fig. 5 shows PL decay kinetics of LiAF crystals recorded at $T = 7.2$ K monitoring emissions at $\lambda_m = 440$ and 340 nm upon VUV-excitations at different energies $E_{ex}$. From Fig. 5 it follows that PL decay kinetics is different for each of the PL emission bands and it depends also on $E_{ex}$. The experimental equipment did not allowed us to measure the PL decay components with lifetimes of the microsecond time-range. Such long decaying components were apparent in our measurements in the form of a constant level — pedestal. Such a way, PL decay kinetics recorded at $\lambda_m = 340$ nm,

$E_{ex} = 6.2$–6.8 eV, is dominated by a fast nanosecond ($\tau = 3.2$ ns) component with contribution of 90–97% that manifests itself on the pedestal of the slow decaying component with lifetime of microsecond time-range. At $E_{ex} > 11.8$ eV, the pedestal dominates with the contribution of 65–75%, whereas the contribution of the fast component ($\tau = 9.6$ ns) decreased accordingly. Qualitatively similar picture is observed for PL decay kinetics recorded at $\lambda_m = 440$ nm. However, the pedestal contributes 50% even at $E_{ex} = 6.2$ eV. At the further increase in energy $E_{ex}$ to 10.78 eV, the contribution of the nanosecond component ($\tau = 10.2$ ns) remains practically unchanged.

Fig. 6 shows time-resolved PL emission spectra of LiAF crystals recorded at $T = 300$ K monitoring emission within time-window 1–6 ns using SR-excitation pulses with the 10 ns repetition period. The PL emission spectra are recorded in a wide UV–VUV spectral range upon VUV-excitation at different energies $E_{ex}$. To exclude the contribution of the scattered light, the PL emission spectra were recorded monitoring emission within time window of 1–6 ns, which means the 5 ns-wide time-window delayed by 1 ns relative to the arrival of SR-excitation pulses. It is quite clear that the long-wavelength emission bands at $\lambda_m > 300$ nm do not show significant intensity in the PL emission spectrum. Therefore, the photoluminescence yield for long-wavelength emission bands at room temperature undergoes thermal quenching. At the same time, it was revealed that VUV–UV luminescence yield decreases with decreasing temperature. However, a study of the temperature dependence of the PL emission of LiAF crystals in a wide spectral range is not a subject of this research work. The most important result follows from Fig. 6: there are two intense VUV–UV emission bands at 170 nm (7.28 eV) and 208 nm (5.96 eV), which dominate the PL emission spectrum at 300 K.

Fig. 7 shows PLE-spectra of LiAF crystals recorded at $T = 300$ K monitoring emissions in the UV–VUV energy range. The PLE spectrum recorded monitoring emission at $\lambda_m = 208$ nm (UV-emission band) comprises three PLE bands at 8.02, 8.7 and 10.5 eV, Fig. 7 (plot 2). When $\lambda_m$ is changed to 170 nm, only two PLE-bands at 8.02 and 8.7 eV remain. An increase in energy $E_{ex}$ above 9 eV leads to a sharp drop in the PL output (Fig. 7, plot 1). Therefore the PLE-spectra of VUV bands (Fig. 7) differ considerably from PLE-spectra for long-wavelength bands at 450 and 320–340 nm, Fig. 4.

### 3.2. Soft X-ray excitation

Fig. 8 shows PL emission spectra of LiAF crystals recorded at $T = 300$ K monitoring emission in time-integrated mode (TI), and within time-windows $TW_1$ and $TW_2$ upon XUV excitation at

**Table 2**
Fractional atomic coordinates $(x, y, z)$ and isotropic displacement $(B_{iso})$ (Å) for LiAF.

| Atom | $x$ | $y$ | $z$ | $B_{iso}$ |
|---|---|---|---|---|
| Li1 | 0 | 0.164(6) | 0.25 | 3.0(12) |
| Li2 | 0.298(2) | 0.338(4) | 0.589(3) | 1.0(6) |
| Li3 | 0.315(2) | 0.205(3) | 0.922(3) | 1.7(6) |
| Li4 | 0.0473(19) | 0.337(4) | 0.531(3) | 2.1(7) |
| Li5 | 0.1488(17) | 0.857(3) | 0.266(3) | 1.0(6) |
| Al1 | 0 | 0 | 0 | 1.33(19) |
| Al2 | 0.3366(4) | 0.0091(11) | 0.7004(4) | 1.27(14) |
| F1 | 0.0952(6) | 0.3431(14) | 0.1995(9) | 2.00(12) |
| F2 | 0.2297(5) | 0.3477(13) | 0.8815(8) | 2.00(12) |
| F3 | 0.1033(6) | 0.3419(13) | 0.6989(9) | 2.00(12) |
| F4 | 0.2512(5) | 0.0154(12) | 0.8280(7) | 2.00(12) |
| F5 | 0.0778(6) | 0.1548(11) | 0.9403(8) | 2.00(12) |
| F6 | 0.9361(6) | 0.1637(11) | 0.0595(9) | 2.00(12) |
| F7 | 0.4220(5) | 0.9777(10) | 0.5687(8) | 2.00(12) |
| F8 | 0.2637(6) | 0.1505(13) | 0.6039(8) | 2.00(12) |
| F9 | 0.0706(5) | 0.0086(14) | 0.1588(6) | 2.00(12) |

**Table 3**
Lengths of the principal bonds (Å) for LiAF.

| Bond | Length | Bond | Length |
|---|---|---|---|
| Li1–F1 | 2.11(4) | Li4–F7 | 1.91(3) |
| Li1–F6 | 2.032(9) | Li4–F7 | 2.19(3) |
| Li1–F9 | 1.91(3) | Li5–F2 | 2.32(3) |
| Li2–F4 | 1.87(3) | Li5–F3 | 1.89(3) |
| Li2–F6 | 2.01(3) | Li5–F4 | 1.88(3) |
| Li2–F8 | 1.66(3) | Li5–F5 | 2.06(3) |
| Li2–F8 | 2.04(3) | Li5–F8 | 2.37(3) |
| Li3–Li | 2.60(4) | Li5–F9 | 1.96(3) |
| Li3–F1 | 1.86(3) | Al1–F5 | 1.833(9) |
| Li3–F2 | 1.73(3) | Al1–F6 | 1.772(9) |
| Li3–F2 | 2.13(3) | Al1–F9 | 1.804(6) |
| Li3–F4 | 2.02(3) | Al2–F1 | 1.824(12) |
| Li3–F5 | 2.30(3) | Al2–F2 | 1.810(12) |
| Li3–F7 | 2.55(3) | Al2–F3 | 1.891(12) |
| Li4–F3 | 1.79(3) | Al2–F4 | 1.812(8) |
| Li4–F5 | 2.38(3) | Al2–F7 | 1.862(8) |
| Li4–F6 | 1.74(3) | Al2–F8 | 1.805(12) |
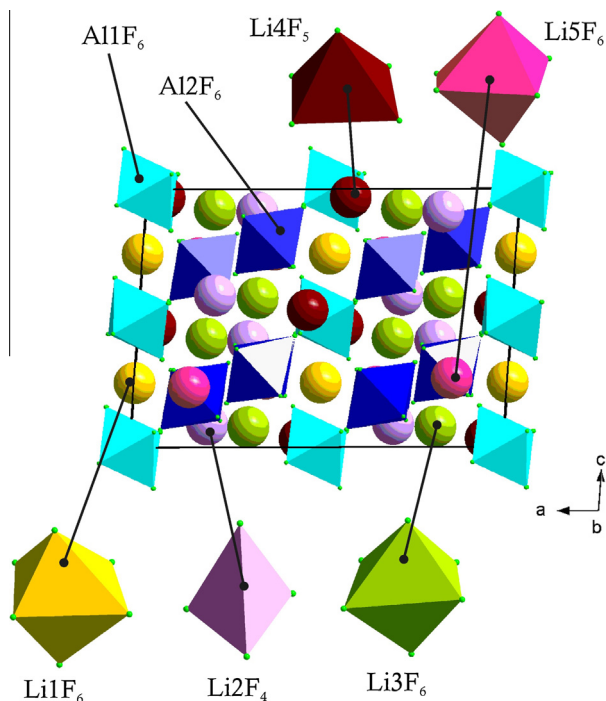
**Fig. 2.** Crystal structure of LiAF.
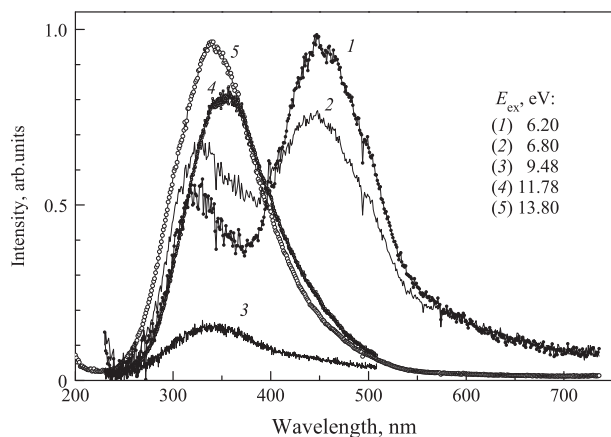


**Fig. 3.** PL emission spectra of LiAF crystals recorded at $T$ = 7.2 K using CCD-camera upon VUV-excitation at different energies $E_{ex}$.



**Fig. 4.** PL excitation spectra of LiAF crystals recorded at $T$ = 7.2 K monitoring emission at $\lambda_m$ = 440 (a) and 340 nm (b) in time-integrated mode TI (1), and within time-windows TW$_1$ (2), and TW$_2$ (3). Each curve is normalized to unity at the maximum of intensity.



**Fig. 5.** PL decay kinetics of LiAF crystals recorded at $T$ = 7.2 K monitoring emission at $\lambda_m$ = 440 (a) and 340 nm (b) upon VUV excitation at different energies $E_{ex}$.

$E_{ex}$ = 130 eV. The PL emission spectra were recorded in a wide VUV-UV–VIS spectral region and they cover both the long-wavelength bands at 320–325 and 450 nm, and the UV–VUV bands I and II. At a qualitative level, the PL emission spectra registered upon soft X-ray excitation perfectly correlate with the above results obtained by VUV excitation. We observe the same relatively narrow bands at 170 (I) and 208 nm (II) in the VUV–UV spectral region and the broader long-wavelength bands at 320 and 440 nm. However, the relative intensities of the PL emission bands recorded upon VUV- and XUV-excitations are different that naturally should be associated with such methods of PL excitations: intracenter (VUV) and recombination (XUV) PLE-mechanisms.

Fig. 9 shows PL decay kinetics of LiAF crystals recorded at $T$ = 300 K monitoring emissions at $\lambda_m$ = 440 and 320 nm upon XUV-excitations at $E_{ex}$ =130 nm. It is worth noting that the VUV–UV emission bands exhibit mainly a pedestal – slowly decaying components with lifetimes in the micro- and possibly millisecond time-range. From Fig. 9 it follows that the PL decay kinetics of the
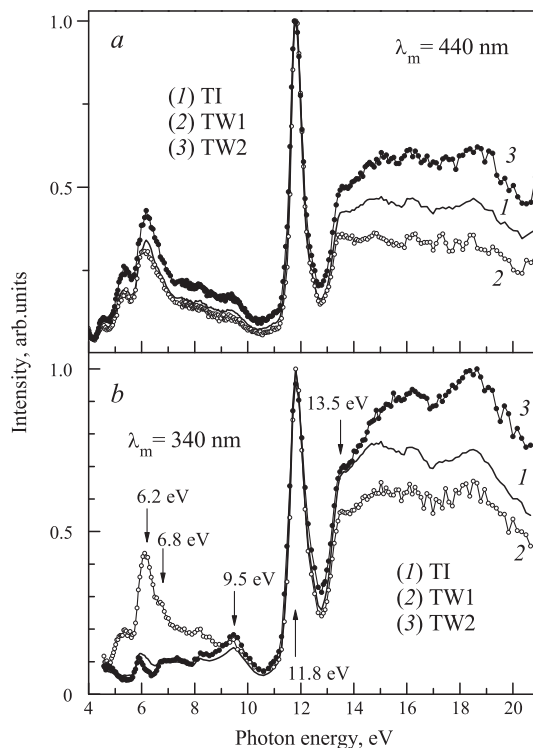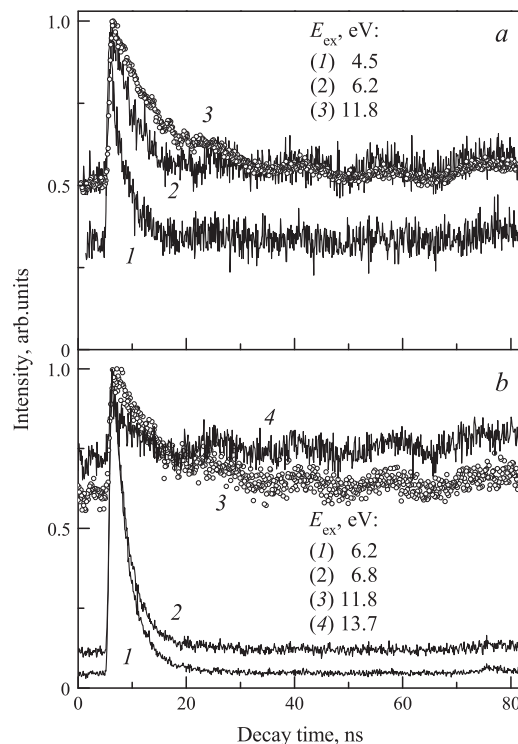
long-wavelength emission band comprises a fast nanosecond component with lifetime $\tau$ = 3.8 ns, which contributes 94% and dominates the $\lambda_m$ = 440 nm emission band. When $\lambda_m$ changes to
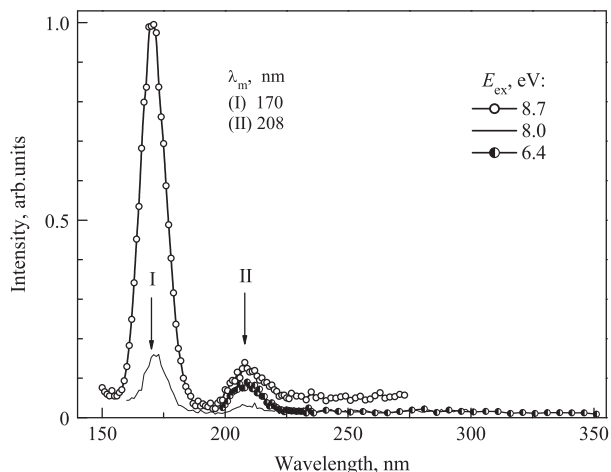
**Fig. 6.** Time-resolved PL emission spectra of LiAF crystals recorded at $T = 300$ K monitoring emission within time-window of 1–6 ns using SR-excitation pulses with the 10 ns repetition period.
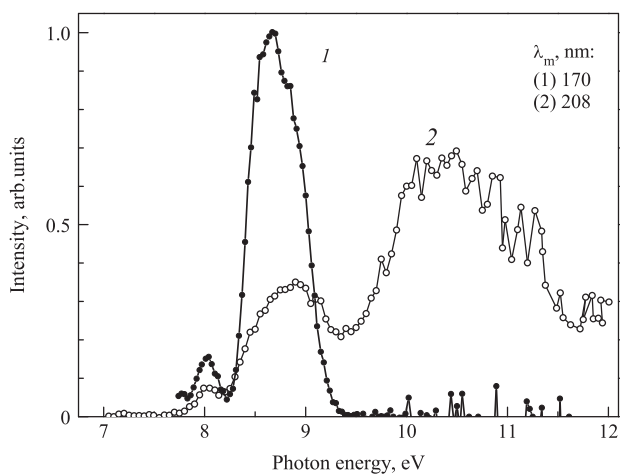


**Fig. 7.** PLE spectra of LiAF crystals recorded at $T = 300$ K monitoring emission at $\lambda_m = 170$ and 208 nm within time-window 1–6 ns. Curve (*1*) is normalized to unity at the maximum of intensity, whereas curve (*2*) is normalized arbitrary for better viewing.
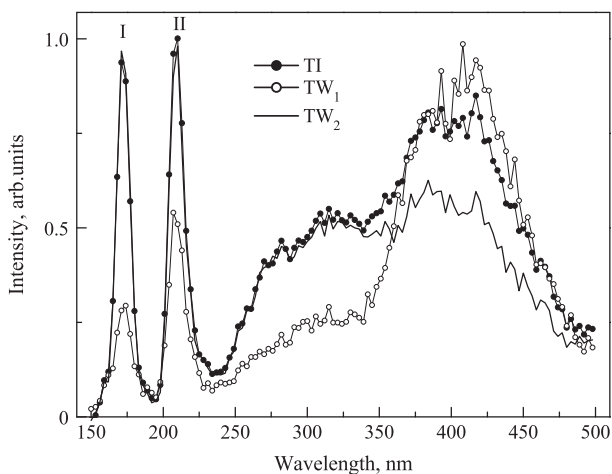


**Fig. 8.** Time-resolved PL emission spectra of LiAF crystals recorded at $T = 300$ K monitoring emissions in time-integrated mode TI, and within time-windows TW$_1$ (2), and TW$_2$ upon excitation at $E_{ex} = 130$ eV. Experimental points are connected by straight line segments for better viewing. Each curve is normalized to unity at the maximum of intensity.
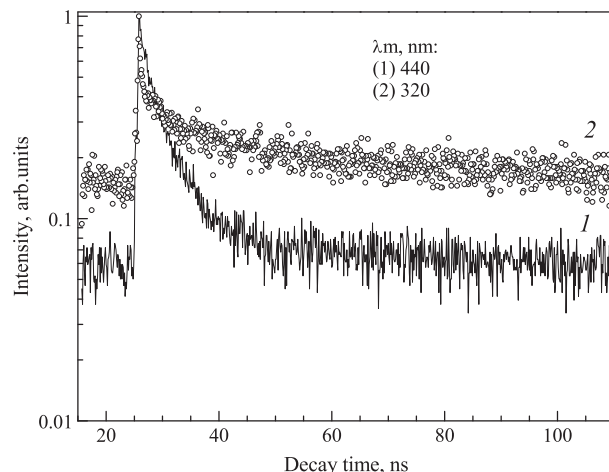


**Fig. 9.** PL decay kinetics of LiAF crystals recorded at $T = 300$ K monitoring emission at $\lambda_m = 440$ and 320 nm upon XUV excitation at $E_{ex} = 130$ eV.

320 nm, then the pedestal is preserved, but the contribution of the fast nanosecond component is reduced to 75%.

## 4. Discussion

### 4.1. Electronic structure parameters

The usual way to obtain the electronic structure parameters from the VUV-spectroscopy technique is the study of the reflection spectra followed by a dispersion analysis, or Kramers-Krönig transform. The reflection spectra of many ionic crystals in this regard are well studied, e.g. [26,27]. Unfortunately, the grown LiAF polycrystalline samples do not have a form suitable for the study of the reflection spectra. In this regard, some electronic structure parameters could be derived solely from the results of the luminescent spectroscopy, Figs. 4 and 7.

We are not aware of experimental data on optical absorption at the low-energy tail of the LiAF host absorption, but there are data available on related crystals. The values of low-temperature band-gap width for these crystals are: $E_g = 12.3$ eV for LiBAF [17]; $E_g = 12.65$ eV for LiCAF [12]; $E_g = 10.8$ eV for AlF$_3$ [28]. The energy threshold for the excitation of anionic exciton in LiBAF is $E_n = 11.6$ eV [17]. In this context, the energy interval of 10.5–12.5 eV is a reasonable estimate for the low-energy edge of the LiAF host absorption.

There is a narrow peak at $E_{ex} = 11.8$ eV in the PLE-spectra of LiAF crystals at $T = 7.2$ K (Fig. 4), which not only falls within this energy range, but manifests all signs of an excitation peak of 'excitonic' luminescence. If this assumption is correct, the profile of this peak at 11.8 eV in PLE-spectra (Fig. 4) is caused by two competing processes. In the framework of simple diffusion concepts [29,30], the low-energy slope of the PLE-peak is due to an increase in the optical absorption coefficient $\mu(E)$ in the range of several tens of cm$^{-1}$, which occurs at the low-energy tail of the host absorption. High-energy slope of the PLE-peak corresponds to a further increase in $\mu(E)$ resulting in the surface energy losses. This leads to a decrease in PLE-efficiency in the energy range of 11.8–12.8 eV. The sharp increase in PLE-efficiency, in the energy range of 12.8–13.5 eV, should be attributed to interband transitions. From Fig. 4 it can be seen that the $E_g \approx 12.5$ eV is quite reasonable estimate for the cut-off energy of PLE-spectrum at the Urbach tail. This interpretation of PLE-spectrum suggests that LiAF-crystal has a mobile electronic excitations – excitons. From theoretical concepts [29,30] it follows that the excitonic absorption peak

($E_n$) should be localized in the energy range of $E_{ex} < E_n < E_g$. This corresponds to a reasonable estimate: 11.8 eV < $E_n$ < 12.5 eV.

## 4.2. Excitonic luminescence

In spite of the approximate nature of the electronic structure parameters derived in the previous section, they allow us to consistently interpret the experimental data on the luminescence of LiAF crystals.

PL emission band peaking at 320–350 nm is complex in origin. The long-wavelength part of this band peaking at 340–350 nm (Fig. 3, curve 4), can most efficiently be excited at the low-energy tail of the host absorption at $E_{ex}$ = 11.8 eV. The most likely interpretation of the PL band at 340–350 nm is the following. We believe that the photoexcitation at the long-wavelength tail of the LiAF host absorption leads to the creation of unrelaxed excitons. The most probable decay channels for the excitons are: migration, followed by non-radiative decay; self-trapping, followed by radiative annihilation; and dissociation into an electron and a hole with the possible participation of the latter in the recombination process. Let us discuss the decay channels of unrelaxed excitons considering the experimental data.

Migration and non-radiative decay at the surface are responsible for the surface energy losses. PLE-spectra of LiAF, recorded at $T$ = 7.2 K monitoring emission at 340–350 nm, have a well-resolved dominant peak in the excitonic energy region at $E_{ex}$ = 11.8 eV, Fig. 4. The presence of this narrow peak may indicate an excitonic mechanism of energy transfer in LiAF, which is typical for systems where luminescence is either excitonic in origin, or excitons are the intermediary in the energy transfer to emission centers. The excitonic origin of the spectral shape for the PLE peak at $E_{ex}$ = 11.8 eV has been discussed above.

The second channel of excitonic decay is a self-trapping and subsequent radiative annihilation of self-trapped exciton (STE). The results of this research work together with the published data on the various fluorides, e.g. [12,17,31], revealed the characteristic features of the short-wavelength broadband luminescence in the crystals: among them, a fairly high quantum yield; a large Stokes shift; the absence of selective excitation bands in the optical transparency region; the presence of exponential component in the PL decay kinetics; efficient PL-excitation in the energy range of excitonic absorption; freezing of the efficient energy transfer to the lattice defects. It is known that such a set of properties exhibit STE in alkali halide crystals [32] or wideband low-symmetry oxides, for example, lithium borates [33]. This gives reason to believe that a broad PL emission band in LiAF crystals is due to radiative annihilation of relaxed electronic excitations – STE, whose decay causes luminescence at 340–350 nm. The high efficiency of PL excitation at the low-energy tail of the host absorption indicates that the STE is produced by relaxation of unrelaxed exciton. The absence of 'freezing' of STE emission at low temperatures suggests a lack of self-trapping barrier or its low height, which is typical for many low-symmetry oxide with a complex host lattice.

PLE-spectra recorded at $T$ = 7.2 K monitoring STE-emission (Figs. 4(b) and 8), demonstrate efficient excitation of the luminescence in the energy region above $E_g$. This indicates that the STE excitation occurs in recombination processes. Self-trapped hole in alkali halide crystals is in the form of $V_k$-center, which can act as the hole kernel of STE [32]. Therefore, one of the excitation channels for STE in these crystals is an electronic recombination at $V_k$-centers. We are not aware of publications on $V_k$-centers in LiAF crystals. However, there is convincing evidence of the existence of $V_k$-centers and recombination processes with their participation in the related complex fluoride crystals [31], in particular LiBaF$_3$ crystals. Self-trapping of holes in LiBaF$_3$ crystals occurs in the form of

fluorine $F_2^-$, molecular $V_k$-centers occupying the fluorine site and oriented along [110] direction [34]. The thermally stimulated migration of the $V_k$-center occurs starting from $T$ = 100 K via reorientation hops, without breaking the molecular bond; above $T$ = 130 K the $V_k$-center are thermally destroyed [35,36].

## 4.3. Defect luminescence

PL emission band at 450 nm and short-wavelength part of the complex PL emission band with maximum at 320–325 nm can be excited in the energy range well-below $E_n$, Fig. 3 (curves 1, 2), so they should be attributed to the PL emission of defects. This explains the direct photoexcitation of these bands at 6.2–6.8 eV, Fig. 3. The presence of defects makes it possible to transfer of excitation energy to the emission centers through the migration of excitons. Alternatively, formation of near-defect excitons with subsequent relaxation and radiative decay in the vicinity of the defects may also occur. This explains the excitation of defect emission in PLE-energy range, where the creation of unrelaxed excitons occurs. The available experimental data do not allow us at this stage to discuss the origins of these defects in LiAF. However, related LiBaF$_3$ crystal has been investigated in this regard and there are extensive data on lattice defects and recombination processes. Let's discuss them briefly.

Electronic F-type color centers in pure LiBaF$_3$ have been studied by electron paramagnetic resonance (EPR) technique [37–39], optical spectroscopy [40–42], trap spectroscopy [43–45]. The luminescence bands at 300–370 nm in LiBaF$_3$ was attributed to charge transfer transitions between F-type and $V_k$ centers [35,36].

The above results show that defect PL emission bands at 320–325 and 450 nm in LiAF have many properties in common with those of LiBaF$_3$. We believe that further study of the origin of intrinsic lattice defects in LiAF (F-type and $V_k$ centers) will allow us to explain the origin of the defect PL emission bands at 320–325 and 450 nm similar to those for LiBaF$_3$.

PL emission bands in the UV–VUV energy at 170 and 208 nm (Fig. 6) were registered upon the excitation at the optical transparency region of LiAF crystals (Fig. 7), so they are also caused by defect emission. The available experimental data do not allow us to give a final interpretation of their origin yet. At this stage, we can only make a reasonable assumption that the UV–VUV luminescence at 170 and 208 nm revealed for LiAF crystals at 300 K can be attributed to interconfigurational 5d–4f radiative transitions in unintentionally introduced Er$^{3+}$, or Tm$^{3+}$ impurity ions. It is worth noting that in the related LiCAF crystals at 300 K exhibit luminescence in the spectral range of 160–210 nm, due to 5d–4f transitions in Er$^{3+}$, or Tm$^{3+}$: the shortest- wavelength peak at 163–165 nm dominates PL emission spectrum, while other peaks in the spectral range of 180–210 nm are one order of magnitude lower in intensity [46]. This is quite consistent with our data for LiAF. Moreover, PLE-band at 8.7 eV (FWHM = 0.6 eV) in LiAF crystals (Fig. 7) recorded monitoring emissions at 170 or 208 nm, coincides with the wavelength $h\nu$ = 140 nm (8.8 eV) used to excite 5d–4f emission from Er$^{3+}$ and Tm$^{3+}$ in LiCAF [46] and certain other fluoride crystals [47,48]. Relatively broadband luminescence at 163–165 nm in LiCAF had shortest wavelength among the fluoride crystal hosts ever reported at room temperature experiments. It is important that UV–VUV luminescence at 170 nm, recorded for LiAF crystals at 300 K, has substantially identical characteristics. This opens up the possibility of using VUV-luminescence of LiAF crystals in scintillators for radiation detectors, which employ photosensitive gases or photocathodes sensitive mostly to VUV photons. The unidentified impurity phase detected by XRD technique (see Section 2.2) could be closely connected with the presence of these impurities. As the rare-earth ions RE$^{3+}$ are substantially

larger in size compared with equally charged host cations $Al^+$, the unintentional doping could lead to the foreign phase formation as it was revealed for LiBAF in [16].

## 5. Conclusions

Thus, for the first time we have carried out a photoluminescence study for monoclinic LiAF crystals upon VUV- and XUV-excitations, using the low-temperature ($T$ = 7.2 K) time-resolved spectroscopy technique. The main conclusions are as follows.

Using Bridgman technique we have grown LiAF crystals suitable for optical studies. All the crystals were found $\beta$-LiAF with lattice parameters $a$ = 14.2292(7); $b$ = 8.4038(5); $c$ = 9.8800(5) Å; $\beta$ = 94.078(2)°. Low-temperature ($T$ = 7.2 K) PL emission spectra with time-resolution revealed the intrinsic PL emission band at 340–350 nm, which was ascribed to radiative annihilation of self-trapped excitons. Other bands at $\lambda_m$ = 320–325 and 450 nm were attributed to luminescence caused by lattice defects. PLE-bands due to the creation of unrelaxed excitons were identified at $E_{ex}$ = 11.8 eV. PLE-spectra analysis gave estimates of the electronic structure parameters at $T$ = 7.2 K: bandgap $E_g \approx 12.5$ eV, energy threshold for creation of unrelaxed excitons $11.8\ eV < E_n < 12.5\ eV$. We found efficient excitation of PL emission bands in the energy range of interband transitions ($E_{ex} > 13.5$ eV) and in the range of core transitions at 130 eV. In the PL spectra recorded at 300 K we have found extrinsic UV–VUV PL bands at 170 and 208 nm. We expressed a reasonable assumption that these bands originate from interconfigurational 5d–4f radiative transitions in unintentionally introduced $Er^{3+}$ or $Tm^{3+}$ impurity ions. As far as we are aware, the UV–VUV emission in LiAF has shortest wavelength after LiCAF among the fluoride crystal hosts ever reported at room temperature experiments.

## Acknowledgments

## References

[1] J.H. Burns, A.C. Tennissen, G.D. Brunton, Acta Crystallogr. B 24 (2) (1968) 225–230.
[2] G. Garton, B. Wanklyn, J. Inorg. Nucl. Chem. 27 (11) (1965) 2466–2469.
[3] M. Hamadàne, J. Grannec, A. Guehria, J. Ravez, Phase Transit. 73 (3) (2001) 423–437.
[4] A.K. Tyagi, J.R. Köhler, Mater. Res. Bull. 32 (12) (1997) 1683–1689.
[5] I. Koštenská, J. Vrbenská, M. Malinovský, Chem. Zvesti 27 (3) (1973) 296–300.
[6] G.T. Furukawa, W.G. Saba, J.C. Ford, J. Res. Nat. Bur. Stand. (US) 74A (5) (1970) 631–639.
[7] P. Fellner, S. Midtlyng, A. Sterten, J. Thonstad, J. Appl. Electrochem. 23 (1) (1993) 78–81.
[8] R. Miyazaki, H. Maekawa, ECS Electrochem. Lett. 1 (6) (2012) A87–A89.
[9] A.A. Merkulov, L.I. Isaenko, S.I. Lobanov, D.Y. Naumov, N.V. Kuratieva, Acta Crystallogr. C64 (7) (2008) i66–i68.
[10] S.I. Omelkov, M. Kirm, E. Feldbach, V.A. Pustovarov, S.O. Cholakh, L.I. Isaenko, J. Phys.: Condens. Matter 22 (29) (2010) 295504.
[11] I.N. Ogorodnikov, S.I. Omelkov, V.A. Pustovarov, A. Kasikov, M. Kirm, Opt. Mater. 39 (2015) 52–57.
[12] M. Kirm, M. True, S. Vielhauer, G. Zimmerer, N.V. Shiran, I. Shpinkov, D. Spassky, K. Shimamura, N. Ichinose, Nucl. Instrum. Meth. Phys. Res. A 537 (2005) 291–294.
[13] C.D. Marshall, S.A. Payne, J.A. Spaeth, W.F. Krupke, G.J. Quarles, V. Castillo, B.H.T. Chai, J. Opt. Soc. Am. B-Opt. Phys. 11 (10) (1994) 2054–2065.
[14] N. Shiran, A. Gektin, S. Neicheva, M. Weber, S. Derenzo, M. Kirm, M. True, I. Shpinkov, D. Spassky, K. Shimamura, N. Ichinose, Nucl. Instrum. Meth. Phys. Res. A 537 (2005) 266–270.
[15] M.N. Sanz-Ortiz, F. Rodriguez, R. Valiente, J. Phys.: Condens. Matter 22 (12) (2010) 125502.
[16] S.I. Omelkov, V. Kiisk, I. Sildos, M. Kirm, V. Nagirnyi, V.A. Pustovarov, L.I. Isaenko, S.I. Lobanov, Radiat. Meas. 56 (2013) 49–53.
[17] V.A. Pustovarov, I.N. Ogorodnikov, S.I. Omelkov, D.A. Spassky, L.I. Isaenko, J. Opt. Soc. Am. B-Opt. Phys. 31 (8) (2014) 1926–1934.
[18] M.H. Du, D.J. Singh, J. Appl. Phys. 112 (2012) 123516.
[19] M.H. Du, D.J. Singh, Proc. SPIE 8852 (2013) 885205.
[20] A.A. Mubarak, A.A. Mousa, Comput. Mater. Sci. 59 (2012) 6–13.
[21] M.J. Knitel, P. Dorenbos, J.T.M. De Haas, C.W.E. van Eijk, LiBaF₃, A scintillator for thermal-neutron detection with optimal $n$-gamma discrimination, in: Proceedings of the International Conference on Inorganic Scintillators and Their Applications, Delft University Press, Delft, 1995, pp. 81–83.
[22] M. Kirm, A. Lushchik, Ch. Lushchik, S. Vielhauer, G. Zimmerer, J. Lumin. 102–103 (2003) 307–312.
[23] G. Zimmerer, Radiat. Meas. 42 (4–5) (2007) 859–864.
[24] T. Balasubramanian, B. Jensen, S. Urpelainen, B. Sommarin, U. Johansson, M. Huttula, R. Sankar, E. Nõmmiste, S. Aksela, H. Aksela, R. Nyholm, AIP Conf. Proc. 1234 (2010) 661–664.
[25] Bruker AXS, Karlsruhe, Germany, TOPAS: General Profile and Structure Analysis Software for Powder Diffraction Data, v4.2, 2009.
[26] G.W. Rubloff, J. Freeouf, H. Fritzsche, K. Murase, Phys. Rev. Lett. 27 (6) (1971) 1317–1320.
[27] G.W. Rubloff, Phys. Rev. B: Condens. Matter 5 (2) (1972) 662–684.
[28] D. König, G. Ebest, Solid-State Electron. 44 (1) (2000) 111–116.
[29] A.N. Vasil'ev, V.V. Mikhailin, Introduction in Solid State Spectroscopy, Moscow University Press, Moscow, 1987.
[30] A. Belsky, J.C. Krupa, Displays 19 (1999) 185–196.
[31] J.H. Beaumont, W. Hayes, D.L. Kirk, G.P. Summers, Proc. Roy. Soc. London. A 315 (1520) (1970) 69–97.
[32] Ch. B. Lushchik, Free and self-trapped excitons in alkali halides: spectra and dynamics, in: E. Rashba, M. Sturge (Eds.), Excitons, Publ. Conf., North-Holland, 1982, pp. 506–541.
[33] I.N. Ogorodnikov, V.A. Pustovarov, A.V. Kruzhalov, L.I. Isaenko, M. Kirm, G. Zimmerer, Phys. Solid State 42 (3) (2000) 464–472.
[34] K. Somaiah, M.V. Narayana, L.H. Brixner, Mater. Chem. Phys. 24 (4) (1990) 353–562.
[35] I. Tale, H.-J. Fitting, P. Kulis, V. Ogorodnik, U. Rogulis, M. Springis, V. Tale, J. Trokšs, Ā. Veispāls, Radiat. Eff. Defect. Solid. 149 (1–4) (1999) 269–272.
[36] I. Tale, M. Springis, U. Rogulis, V. Ogorodnik, P. Kulis, V. Tale, A. Veispals, H.J. Fitting, Radiat. Meas. 33 (5) (2001) 751–754.
[37] A. Fedotovs, E. Elsts, U. Rogulis, A. Gulans, I. Tale, M. Nikl, N. Ichinose, K. Shimamura, Phys. Status Solidi (c) 4 (3) (2007) 1284–1287.
[38] U. Rogulis, V. Ogorodnik, I. Tale, A. Veispals, Radiat. Eff. Defect. Solid. 157 (6–12) (2002) 699–703.
[39] U. Rogulis, J.-M. Spaeth, I. Tale, M. Nikl, N. Ichinose, K. Shimamura, Radiat. Meas. 38 (4–6) (2004) 663–666.
[40] P. Kulis, I. Tale, M. Springis, U. Rogulis, J. Trokss, A. Veispals, H.-J. Fitting, Radiat. Eff. Defect. Solid. 149 (1–4) (1999) 97–100.
[41] P. Kulis, I. Tale, M. Springis, U. Rogulis, A. Veispals, H.-J. Fitting, Radiat. Eff. Defect. Solid. 155 (1–4) (2001) 77–81.
[42] P. Kulis, M. Springis, I. Tale, Radiat. Eff. Defect. Solid. 157 (6–12) (2002) 737–741.
[43] P. Kulis, I. Tale, G. Rudlof, Radiat. Protect. Dosimetry 100 (1–4) (2002) 167–170.
[44] P. Kulis, I. Tale, I. Gromuls, M. Nikl, N. Ichinose, K. Shimamura, Radiat. Meas. 38 (4–6) (2004) 723–726.
[45] I. Tale, P. Kulis, U. Rogulis, V. Tale, J. Trokss, A. Veispals, M. Barboza-Flores, H.-J. Fitting, J. Lumin. 72–74 (1997) 722–723.
[46] A. Yoshikawa, T. Yanagida, Y. Yokota, A. Yamaji, Y. Fujimoto, J. Pejchal, V.I. Chani, N. Kawaguchi, S. Ishizu, K. Fukuda, T. Suyama, M. Nikl, Opt. Mater. 32 (9) (2010) 845–849.
[47] J. Becker, J.Y. Gesland, N.Yu. Kirikova, J.C. Krupa, V.N. Makhov, M. Runne, M. Queffelec, T.V. Uvarova, G. Zimmerer, J. Lumin. 78 (1998) 91–96.
[48] J. Becker, J.Y. Gesland, N.Yu. Kirikova, J.C. Krupa, V.N. Makhov, M. Runne, M. Queffelec, T.V. Uvarova, G. Zimmerer, J. Alloys Compd. 275–277 (1998) 205–208.
[49] L.B. McCusker, R.B. von Dreele, D.E. Cox, D. Louër, P. Scardi, J. Appl. Cryst. 32 (1999) 36–50.